# Anomalous correlation between thermal conductivity and elastic modulus in two-dimensional hybrid metal halide perovskites

Ankit Negi, Liang Yan, Cong Yang, Yeonju Yu, Doyun Kim, Subhrangsu Mukherjee, Andrew H. Comstock, Saqlain Raza, Ziqi Wang, Dali Sun, Harald Ade, Qing Tu,* Wei You,* and Jun Liu*

A. Negi, C. Yang, S. Raza, Z. Wang, and J. Liu
Department of Mechanical and Aerospace Engineering, North Carolina State University, Raleigh, NC 27695, USA
*Email address: jliu38@ncsu.edu

L. Yan, W. You
Department of Chemistry, University of North Carolina at Chapel Hill, NC 27599, USA
*Email address: wyou@email.unc.edu

Y. Yu, D. Kim, and Q. Tu
Department of Materials Science & Engineering, Texas A&M University, College Station, TX 77843, USA
*Email address: qing.tu@tamu.edu

S. Mukherjee, A.H. Comstock, D. Sun, and H. Ade
Department of Physics, North Carolina State University, Raleigh, NC 27695, USA

A. Negi, L. Yan, C. Yang, S. Mukherjee, A.H. Comstock, S. Raza, Z. Wang, D. Sun, H. Ade, and J. Liu
Organic and Carbon Electronics Laboratories (ORaCEL), North Carolina State University, Raleigh, NC 27695, USA

## Abstract

Device-level implementation of soft materials for energy conversion and thermal management demands a comprehensive understanding of their thermal conductivity and elastic modulus to mitigate thermo-mechanical challenges and ensure long-term stability. Thermal conductivity and elastic modulus are usually positively correlated in soft materials, such as amorphous macromolecules, which poses a challenge to discover materials that are either soft and thermally conductive or hard and thermally insulative. Here, we show anomalous correlations of thermal conductivity and elastic modulus in two-dimensional (2D) hybrid organic-inorganic perovskites (HOIP) by engineering the molecular interaction between organic cations. By replacing conventional alkyl-alkyl and aryl-aryl type organic interactions with mixed alkyl-aryl ones, we observe enhancement in elastic modulus with a reduction in thermal conductivity. This anomalous dependence provides a route to engineer thermal conductivity and elastic modulus independently and a guideline to search for unprecedented thermal management materials. Further,introducing chirality into the organic cation induces a unique molecular packing, leading to the same thermal conductivity and elastic modulus regardless of the composition acrossall half-chiral 2D HOIPs. This finding provides substantial leeway for further investigations in chiral 2D HOIPs to tune optoelectronic properties without compromising the thermal and mechanical stability.

Key words: thermal conductivity, elastic modulus, hybrid perovskite, organic cations, chirality

## 1. Introduction

Thermal and mechanical properties are important considerations when implementing device-level design to mitigate thermo-mechanical challenges and ensure long-term stability.[1–3] A comprehensive understanding of these properties, such as thermal conductivity and elastic modulus, and how they correlate will enable the discovery of novel materials with unprecendental performance. In soft materials, thermal conductivity and elastic modulus are usually positively correlated, particularly when sound velocity plays a dominant role in both properties.[4] In other words, thermal conductivity is higher when the elastic modulus is larger, which has been experimentally demonstrated, such as in polymers[5] and amorphous macromolecules[6,7]. The presence of such a positive correlation poses a challenge in designing novel thermal interface materials capable of dissipating excess heat while maintaining compliance at the same time, or thermal-insulating coating materials that can be thermally insulative and hard simultaneously.

Complex crystals, such as hybrid organic-inorganic materials, offer opportunities to provide an anomalous correlation in thermal conductivity and elastic modulus, due to their tailorable and complex local bonding environment[8–11]. In this work, we focus on two-dimensional (2D) hybrid organic-inorganic perovskite (HOIP), shown in **Figure 1(a)**. In a typical perovskite structure ($ABX_3$), if the A-site is a relatively large-sized organic cation (e.g., long chained alkylamines), a quasi-2D layered structure will form, where one or multiple B-X inorganic octahedron layers are separated by the weakly bonded organic spacers.[12,13] The chemical and structural diversity in HOIPs offers a wide range of possibilities for tuning their physical properties and tailoring them for specific applications by judiciously engineering either the organic or inorganic components.[14–21] However, an anomalous correlation of thermal conductivity and elastic modulus has not yet been found in HOIPs so far. For example, in the study of 3D HOIPs, a positive correlation between thermal conductivity and elastic modulus is still observed upon varying the inorganic composition[22]. Similar behavior between the two properties is also observed in the case of 2D HOIPs with alkyl-type ligands (composed of carbon-carbon chains), where both properties increase with decreasing length of organic ligands.[23,24]

The universality of this correlation in HOIPs cannot be assumed without understanding how both properties depend on different types of organic-organic interfaces, beyond a typical *alkyl-alkyl* type of interface with only van der Waals interactions.[25] If aryl ligands are introduced into the structure, there will be π-π and CH-π interactions at the organic-organic interface.[26,27] Our recent simulation work suggests that π-π stacking enhances the interaction strength of this interface but decreases the thermal transport capability across the interface, which could potentially induce an anomalous correlation between elastic modulus and thermal conductivity.[28] Synthetically, this has been made possible by replacing an existing alkyl cation with an aryl one. For instance, substituting 50% of phenethylammonium (PEA) cations in phenethylammonium lead iodide ($[PEA]_2PbI_4$) with butylammonium ($C_4A$ or BA) results in a mixed metal halide perovskite $[C_4A][PEA]PbI_4$. These so-called mixed 2D HOIPs exhibit unique and tunable interactions between organic cations (i.e., π-π and CH-π interactions), which has been utilized to modulate properties.[27,29–31] Another way of tuning the organic-organic interaction is by introducing chirality into the structure.[32,33] This is facilitated by replacing half or all of the achiral organic ligands with chiral organic ligands. The distortions induced by the chiral molecules cause a reduction in crystal symmetry, which makes them highly appealing for applications such as optoelectronics, bioencoding, spintronics and spin caloritronics, and tomography.[32,34]

Tuning the interaction between organic cations at the organic-organic interface not only offers a relatively less explored, new degree of freedom to alter the 2D HOIP structure (and the properties) but also leads to a more comprehensive understanding of the structure-property relationship.[27] Most experimental thermal transport studies so far are focused on organic cation, inorganic layer thickness, and interlayer distance.[18,35–38] However, there exists a notable gap in understanding the role of the organic-organic interface. Previous investigations into the thermal transport of 2D HOIPs have largely utilized alkyl-type ligands, where van der Waals interactions are the primary bonding forces. Moreover, these studies have been confined to achiral organic cations, limiting the scope for tuning interactions at the organic-organic interfaces. This limitation, particularly in the choice of organic ligands, restricts the bandwidth available for modulating the organic-organic interface.[18,37] Similarly, studies on elastic modulus primarily focus on pure alkyl-alkyl and aryl-aryl type interfaces.[23,39–42] While there is a consensus that the stiffness of the organic cation and the organic-organic interaction play crucial roles in determining the elastic modulus in 2D HOIPs, minimal effort has been dedicated to tuning the latter.[43]To advance our understanding and possibly decouple the thermal and mechanical behavior, there is a need for more comprehensive investigations that delve into the nuanced dynamics of organic-organic interfaces, exploring a broader range of organic cations and interfaces.

Herein, in this work, we prepared 12 different 2D HOIP thin films, modulating the organic-organic interface by using pure achiral, mixed achiral, and chiral organic cations. The chiral 2D HOIP thin films are further classified into two groups, half-chiral (when 50% of the achiral organic cations are replaced with chiral organic cations) and full-chiral (when the entire achiral organic cations are replaced). We measured the thermal conductivity of the spun-cast thin films using the time-domain thermal reflectance (TDTR) method and the elastic modulus using nanoindentation enabled by contact resonance atomic force microscopy (CR-AFM). We discovered an anomalous correlation of thermal conductivity and elastic modulus in mixed achiral 2D HOIPs when replacing the organic cation from a softer alkyl ligand to a more rigid aryl ligand. Moreover, introducing chirality into the organic cation leads to the same thermal conductivity and elastic modulus for all the half-chiral 2D HOIPs, i.e., another anomalous correlation. Using the structural data, grazing-incidence wide-angle X-ray scattering (GIWAXS) characterization, and molecular dynamics (MD) simulations, we explain the observed results and provide insights on the roles of organic-organic interface on modulating the thermal conductivity and elastic modulus of 2D metal halide perovskite thin films. This work provides a route to decouple the dependence of thermal conductivity and elastic modulus on the chemical structure in soft materials and also provides substantial leeway for further investigations in chiral 2D HOIPs to tune opto-electronic properties without affecting the thermal and mechanical stability.

## 2. Results

### 2.1 2D HOIP thin films

A typical lead-halide 2D HOIP system exhibits a sandwich structure, wherein the inorganic $[PbX_6]^{2-}$ networks are sandwiched between two layers of organic ligands.[44] The organic and inorganic ligands are connected via weak interactions such as Coulombic forces of attraction.

This unique structure offers additional knobs for tuning thermal and mechanical properties of the material by modulating the interlayer interactions. **Figure1(a)** shows the typical 2D HOIP structure ($n$=1) comprising alternating layers of inorganic octahedra separated by the weakly bonded organic cations where the inorganic layer, organic layer, inorganic-organic, and organic-organic interfaces could influence material's physical properties. **Figure 1(b)** illustrates the thermal transport pathway in 2D HOIPs. Generally in layered materials, the thermal resistances of the inorganic layer and organic ligands are much smaller compared to those of the inorganic-organic and organic-organic interfaces.[45] For the inorganic-organic interface, changing the halide anion, or in other words, the strength of the electrostatic inorganic-organic interface, does not produce a significant change in the thermal conductivity of 2D HOIPs.[38] Therefore, the organic-organic interface dominates the thermal resistance, and thus thermal conductivity of the material, which is attributed to the nature of the weakly non-bonded interactions. We identify two key parameters that influence the interactions at the organic-organic interface, namely the *spacing* between organic ligands and the *type* of the organic-organic interface, as illustrated in **Figure 1(c)** and **Figure 1(d)**. The interaction at the organic-organic interfaces (e.g., van der Waals or Coulombic interactions) decreases dramatically with an increasing spacing between the non-bonded entities. Further, the non-bonded interaction is heavily influenced by the type of interface. The interaction between alkyl-alkyl interface, dominated by van der Waals interactions is different in comparison to aryl-aryl and aryl-alkyl interfaces, where $\pi$-$\pi$ and CH-$\pi$ interactions play an important role. We prepared 12 2D metal halide HOIP samples (see **Methods** for details) with the type of interface tabulated in **Table 1** and illustrated in **Supplementary Figure S1. Figure 1(e)** shows the different types of organic ligands, including alkyl, aryl, and chiral ones.

**Table 1** Details of the 2D HOIP thin films measured in this work.

| ID | Chirality | Composition | Organic-Organic interface type | Film thickness (nm) | Interlayer distance (Å) |
|---|---|---|---|---|---|
| 1 | Achiral | $[C_4A]_2PbI_4$ | Alkyl-Alkyl | 147.0 ± 11.9 | 13.3 |
| 2 | Mixed achiral | $[C_3A][PEA]PbI_4$ | All three* | 138.0 ± 6.0 | 15.9 ± 0.8$^{\#}$ |
| 3 | Mixed achiral | $[C_4A][PEA]PbI_4$ | All three$^{*}$ | 165.0 ± 3.8 | 16.1 ± 0.8$^{\#}$ |
| 4 | Achiral | $[C_6A]_2PbI_4$ | Alkyl-Alkyl | 148.0 ± 6.0 | 16.5 |
| 5 | Achiral | $[PEA]_2PbI_4$ | Aryl-Aryl | 153.0 ± 1.5 | 16.0 ± 0.8$^{\#}$ |
| 6 | Half-chiral | $[SMePEA][C_3A]PbI_4$ | All three$^{*}$ | 133.0 ± 2.0 | 14.8 ± 0.8$^{\#}$ |
| 7 | Half-chiral | $[SMePEA][C_4A]PbI_4$ | All three$^{*}$ | 145.0 ± 4.0 | 15.8 ± 0.8$^{\#}$ |
| 8 | Half-chiral | $[SMePEA][PEA]PbI_4$ | Aryl-Aryl | 161.0 ± 5.6 | 16.1 ± 0.8$^{\#}$ |
| 9 | Half-chiral | $[SMePEA][C_6A]PbI_4$ | All three$^{*}$ | 146.0 ± 1.0 | 17.1 |

| | | | | | |
|---|---|---|---|---|---|
| 10 | Half-chiral | [SMePEA][$C_8$A]$PbI_4$ | All three* | 151.0 ± 3.0 | 17.6 |
| 11 | Full-chiral | [SMBA]$_2PbI_4$ | Aryl-Aryl | 148.0 ± 2.0 | 14.4 |
| 12 | Full-chiral | [SMePEA]$_2PbI_4$ | Aryl-Aryl | 158.0 ± 2.0 | 17.4# |

* All three organic-organic interfaces including alkyl-alkyl, alkyl-aryl, and aryl-aryl.
\# Interlayer distance characterized using GIWAXS for these 2D HOIP thin films.

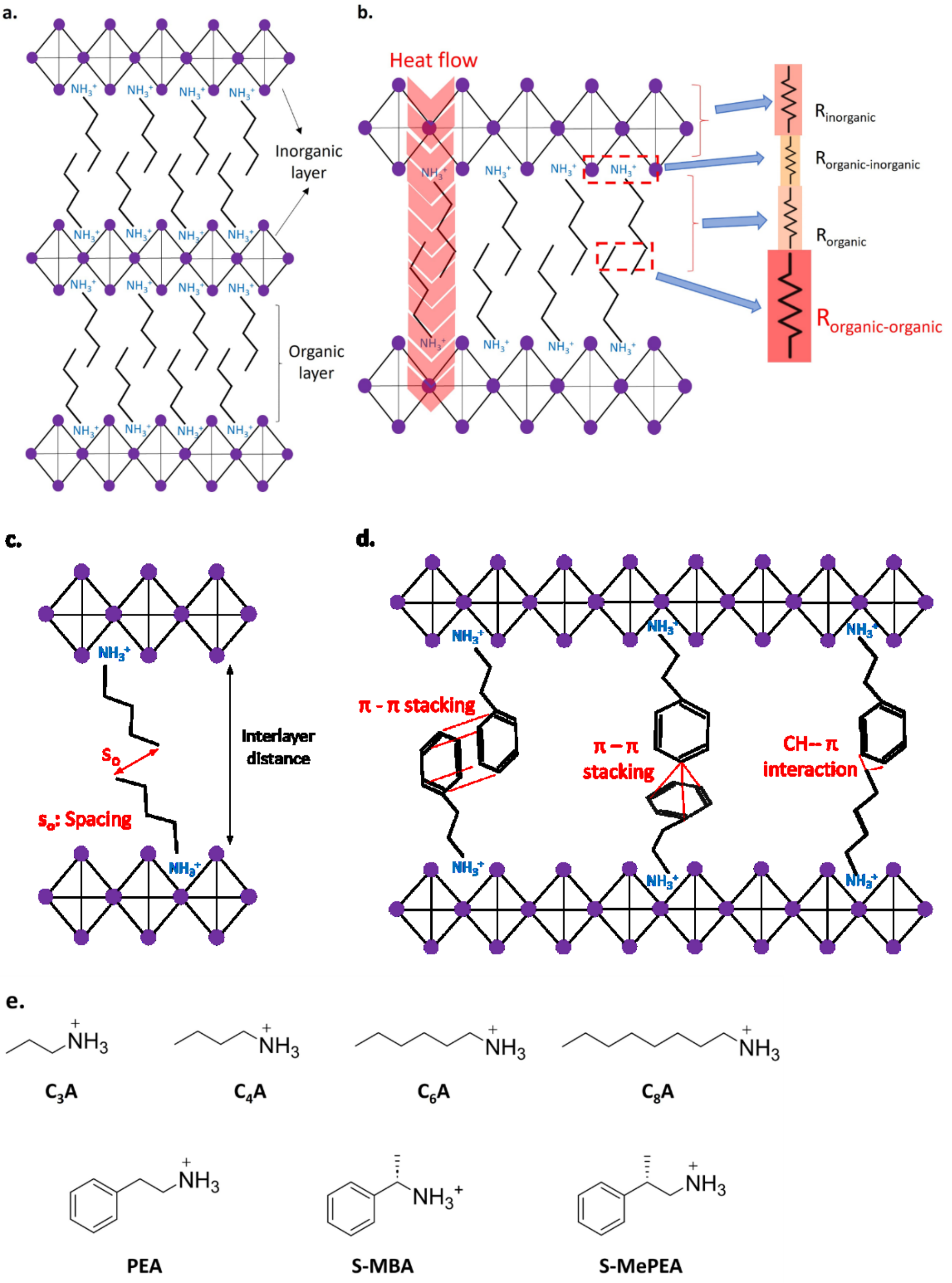

**Figure 1.** Schematics of the chemical structure and composition of 2D metal halide HOIPs. **(a)** Representative 2D HOIP with alkyl-alkyl type organic interface. **(b)** Heat flow and thermal

resistance network for a typical 2D HOIP. Thermal conductivity is largely determined by the organic-organic interface, characterized by the spacing between the organic ligands and the type of the organic-organic interface. The organic interfaces are broadly categorized into three different types namely, **(c)** alkyl-alkyl, **(d)** alkyl-aryl and aryl-aryl, where different interactions between the organic entities beyond van der Waals interactions are indicated in the drawing. The interlayer distance is the separation between the two inorganic layers. **(e)** Organic ligands used in this work. *S* means left-handed chirality.

## 2.2 Thermal conductivity and elastic modulus of 2D HOIP thin films

We measured the cross-plane thermal conductivity of all 2D HOIP thin films using the TDTR method, as shown in **Figure 2(a)**.[46–48] Details of the TDTR method can be found in the **Methods** or our previous publications.[48–50] Prior to the measurements, a thin layer of Cu (≈20 nm) followed by Al (≈80 nm) is coated on all the samples via thermal evaporation. The samples are sealed in a protected Argon gas environment during the measurements, to prevent degradation. The pump laser beam heats the sample and the probe laser beam measures the surface temperature response upon heating with a controllable time delay. Thermal conductivity is obtained by fitting the experimentally obtained normalized temperature rise and decay data (as termed as *Ratio*) with a multi-layered heat conduction model, with geometrical and thermophysical properties of each layer as input parameters and the thermal conductivity of 2D HOIP film as the only fitting parameter. **Figure 2(b)** shows four representative experimental data curve and heat transfer model fitting for the 2D HOIP thin films. Excellent agreement between the experimental data and model is observed for the films used in this study. Detailed sensitivity analysis is presented in the **Supplementary Section S2**. **Figure 2(c)** and **Figure 2(d)** show the thermal conductivity of achiral, mixed-achiral, half-chiral, and full-chiral samples. Comparing the 2D HOIP films with achiral alkyl-alkyl organic interfaces, we see that the thermal conductivity of $[C_4A]_2PbI_4$ is nearly twice that of $[C_6A]_2PbI_4$. Replacing half of the aryl cations in $[PEA]_2PbI_4$ with alkyl cations, such as $[C_3A]$ and $[C_4A]$, increases thermal conductivity. Interestingly, thermal conductivity for all the half-chiral HOIPs is similar, regardless of the achiral organic cation. Thermal conductivity of pure chiral HOIPs (i.e., $[SMBA]_2PbI_4$ and $[SMePEA]_2PbI_4$) is slightly higher than the half-chiral ones.

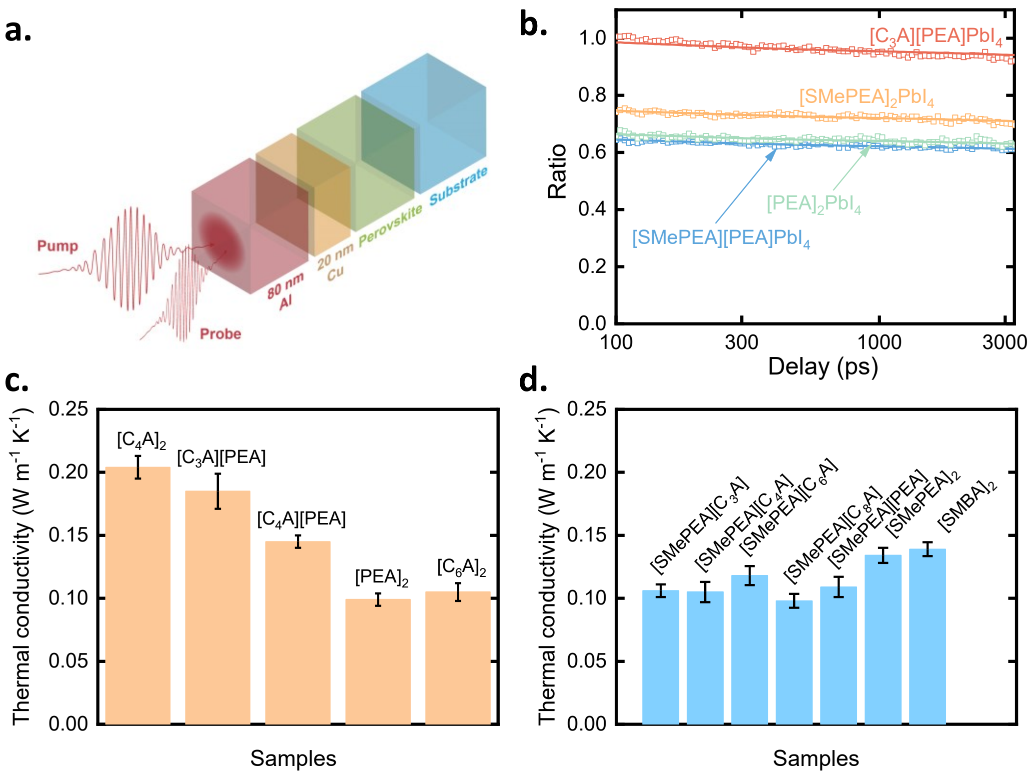

**Figure 2.** Cross-plane thermal conductivity measurement of 2D metal halide HOIP thin films. **(a)** Schematics of TDTR method and sample configuration. **(b)** The TDTR fitting process for the 2D HOIP thin films in this study. The symbols indicate the experimental data and the solid lines show the heat conduction model with fitted thermal conductivity. **(c)** Thermal conductivity of achiral and mixed-achiral samples in this study. **(d)** Thermal conductivity of half-chiral and full-chiral samples in this study. The data is presented in the form of mean value ± standard deviation. The PbI$_4$ is omitted in the labels of (c) and (d) for simplicity.

We also measured the elastic modulus (E) of representative 2D metal halide HOIP thin films using the CR-AFM method. **Figure 3(a)** shows the CR-AFM schematics with details described in the **Methods** section and the **Supplementary Section S3**. **Figure 3(b)** and **Figure 3(c)** show the elastic modulus map and the statistical fitting using normal distribution function, respectively, on a representative sample, [SMePEA][C$_3$A]PbI$_4$. **Figure 3(d)** shows the results of seven selective samples. The CR-AFM measurements of achiral 2D HOIPs show that the highest elastic modulus is for [PEA]$_2$PbI$_4$ thin film (≈12.3 GPa). This result agrees with previous nanoindentation measurements of single crystals, and the high elastic modulus is attributed to the rigidity of the benzene rings and the CH-π interaction.[39,40] Replacing PEA with softer alkyl chains leads to a reduction of elastic modulus in the mixed-achiral 2D HOIP films. And all the mixed-achiral 2D HOIP films have a larger elastic modulus compared to their pure alkyl counterparts (e.g., E≈2.1 GPa for [C$_6$A]PbI$_4$ and E≈3.3 GPa for [C$_4$A]PbI$_4$)[23]. Surpringly, the elastic modulus of [C$_3$A][PEA] is smaller than [C$_4$A][PEA], even though the former carries shorter alkyl chains that should be stiffer (i.e., $E_{C3A} > E_{C4A}$), if extrapolated from the measured trend of elastic modulus's dependence on the chain length between C$_4$ to C$_6$ by nanoindentations.[23,41] Compared to the pure achiral [PEA]$_2$PbI$_4$, the pure chiral [SMePEA]$_2$PbI$_4$ manifests a much lower elastic modulus (≈ 7.3 GPa). We further tested the half-chiral films and found that their elastic moduli are similar within the experimental uncertainty, falling in between 7~9 GPa for all the films.

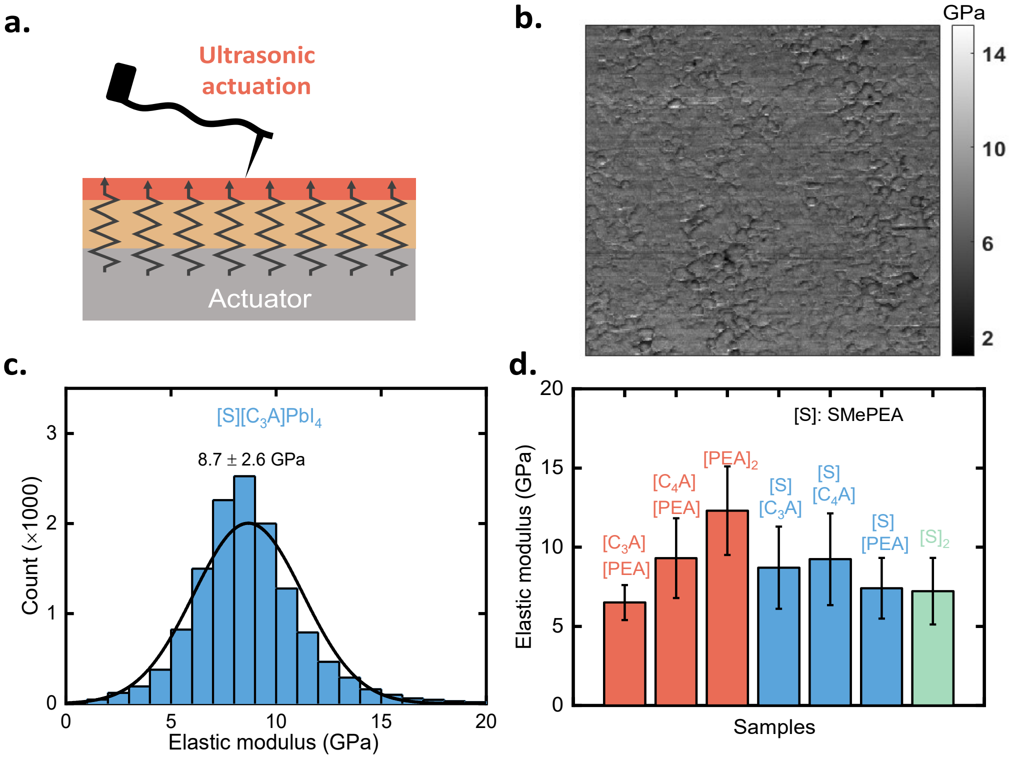

**Figure 3.** Elastic modulus measurement of 2D metal halide HOIP thin films. **(a)** Schematics of the CR-AFM method for elastic modulus map, where the arrows indicate the ultrasonic wave (generated by the actuator) propagating through the sample and drive the AFM cantilever vibration during contact imaging. **(b)** Elastic modulus map of $[SMePEA][C_3A]PbI_4$. The color bar represents elastic modulus in GPa. **(c)** Typical fitting of the measured elastic modulus using normal distribution function measured by CR-AFM for $[SMePEA][C_3A]PbI_4$. **(d)** Elastic modulus of seven representative 2D HOIP thin films. [S] is short for [SMePEA]. The $PbI_4$ is omitted in the labels of (d) for simplicity. The data is presented in the form of mean value ± standard deviation.

### 2.3 Correlation between thermal conductivity and elastic modulus in HOIPs

Significant insights can be obtained by correlating the measured thermal conductivity and elastic modulus of 2D metal halide HOIPs, and comparing with correlations found in the literature. In similar soft materials, including 3D HOIPs, polymers, and amorphous macromolecules, thermal conductivity and elastic modulus are usually correlated by a direct dependence on sound velocity.[5–7,51,52] Elastic modulus is determined by the density and sound velocities of the material. Thermal conductivity is contributed by all the acoustic and optical phonon modes in the material with various travelling speeds and lifetimes. When low-frequency acoustic phonons travelling at the speed of sound with long lifetime channel bulk of the heat in materials, thermal conductivity scales with sound velocity, thus makes it challenging to independently tune thermal conductivity and elastic modulus.[51]

**Figure 4** shows the correlation between thermal conductivity and elastic modulus in HOIPs. We note that the thermal conductivity and elastic modulus measurements are along the vertical direction (perpendicular to inorganic octahedra plane). For 3D HOIPs, where the influence of organic-organic interface is minimal, a positive correlation between thermal conductivity and elastic modulus is established. It is believed that both thermal conductivity and elastic modulus is directly correlated to sound velocity and there is a limited contribution from optical phonons to thermal conductivity due to their lower velocity and shorter lifetime compared to acoustic phonons.[51]

Our results indicate that modulating the organic-organic interface in 2D HOIPs results in an anomalous relation between these two properties. For 2D HOIPs with *alkyl-alkyl* type of interface, we observe a positive correlation between the two properties, similarly as in 3D HOIPs. In 2D HOIPs with *aryl-aryl* and *alkyl-aryl* interfaces, however, we observe an atypical negative correlation. For instance, the thermal conductivity of [$C_3$A][PEA] is larger than [$C_4$A][PEA], while the elastic modulus shows the opposite trend. At the organic-organic interface, elastic modulus is reinforced by the *aryl-aryl* and *alkyl-aryl* interfaces with CH--π and π-π interactions, but the thermal transport is suppressed by these interactions (see detailed analysis in the **Section 3.2 & 3.3**).

Practically, combining the effect of organic cation and the organic-organic interface offers additional “knobs” to engineer thermal and mechanical properties independently. The observed anomalous correlation provides opportunities to decouple thermal conductivity and elastic modulus and potentially lead to engineered *hard but thermally insulative* coating materials. Fundamentally, this finding also challenges the current understanding on thermal transport in 2D HOIPs that appear to coherently transport heat across the organic-organic interface.[24,35] The unusual correlation between thermal conductivity and elastic modulus highlights the importance of optical phonons in regulating room temperature heat flow in 2D HOIPs depending on the interface type.[53,54] Optical phonons may not necessarily contribute to thermal conductivity, but rather provide strong scattering channels for acoustic phonons, as claimed for all-inorganic 2D HOIPs.[55] Another possibility is the large mismatch of phonon spectrum at the *aryl-aryl* and *alkyl-aryl* interfaces induces a strong phonon filtering effect.[28] Indeed, studies on thermal transport in 2D HOIPs have only recently begin to emerge and would require further investigations.

Moreover, the second anomalous observation is that half-chiral 2D HOIPs possess almost the same thermal conductivity and elastic modulus. Fundamentally, this result suggest the unique role of chiral ligands in determining the molecular packing (see discussion in the **Section 3.4**). Practically, this result provides researchers with significant flexibility in adjusting their optoelectronic and structural properties without significantly affecting their thermal and mechanical properties, which is especially critical in device level implementation of these materials when thermo-mechanical failure is a concern.

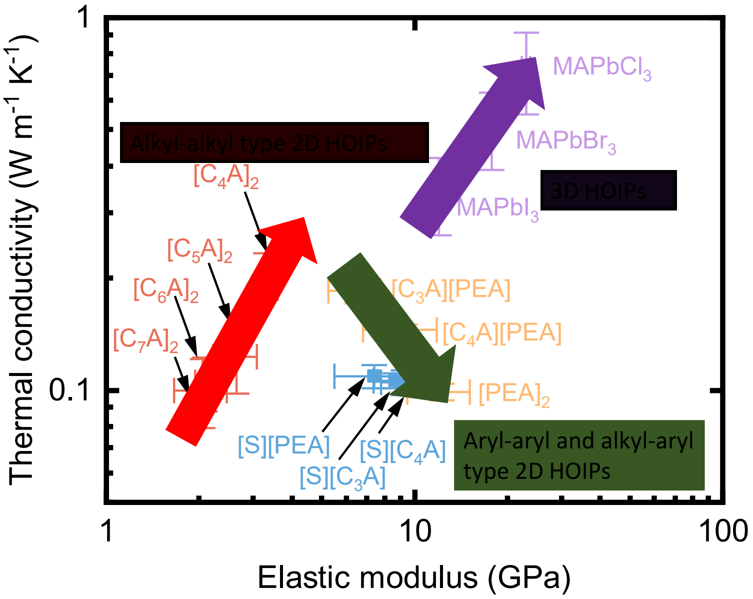

**Figure 4.** Correlation between thermal conductivity and elastic modulus for 3D metal halide HOIPs and 2D metal halide HOIPs with different organic-organic interface types (alkyl-alkyl, alkyl-aryl, and aryl-aryl). The anomalous correlations of thermal conductivity and elastic modulus are shown in solid squares: (1) the mixed achiral 2D HOIPs shows a negative correction (brown); (2) the half chiral 2D HOIPs show constant values of properties (blue). The thermal conductivity and elastic modulus data of 3D HOIPs is taken from Ref. [22], shown in open circles. The thermal conductivity data for [C$_5$A]$_2$PbI$_4$ and [C$_7$A]$_2$PbI$_4$ is taken from Ref. [24], shown in open circles. The elastic modulus data for alkyl-alkyl type 2D HOIPs is taken from Ref. [23]. [S] is short for [SMePEA]. If the inorganic part is not explicitly labeled in the 2D HOIP chemical composition, it is PbI$_4$. Data is presented as mean value ± standard deviation.

## 3. Discussion

To further understand the observed anomalous correlations between thermal conductivity and elastic modulus in 2D HOIPs, we investigate the possible mechanisms by exclusing the effects from crystalline orientation and crystallite size in **Section 3.1** and analyzing each type of organic-organic interfaces in the following sections.

### 3.1 Crystalline orientation and crystallite size analyzed by GIWAXS

In general, both the thermal conductivity and elastic modulus in 2D HOIPs can be modulated by varying the organic cation, the interaction between the two organic cations, and the inorganic framework.[39] As the inorganic layer is the same in all the 2D HOIP films used in this study, the influence of the inorganic layer on thermal conductivity and elastic modulus will be the same. To understand the anomalous correlations between thermal conductivity and elastic modulus in 2D HOIPs in this study, assuming the spun-cast thin film is polycrystalline, we first analyze the crystalline orientation and average crystallite size to eliminate the dependence on these two factors.

GIWAXS analysis was conducted to compare the orientation of the nanocrystals in the thin film and crystallite size among different samples (see **Methods** and **Supplementary Section S4** for details). GIWAXS measures the diffracted intensity of an X-ray beam with an incidence angle close to the total external reflection angle of the 2D HOIP film. Simultaneous measurement of the in-plane and out-of-plane diffraction intensity using a 2D detector allows for the determination of orientational order parameter and crystallite coherent length of the 2D HOIP films. In this study, the orientation of 2D HOIP thin films is quantitively described using the order parameter and the crystallite size is characterized using the coherent length. An order parameter value of unity indicates perfect parallel film orientation relative to substrate (i.e., the inorganic layer is parallel to the substrate) while a value close to zero indicates completely random film orientation relative to substrate.

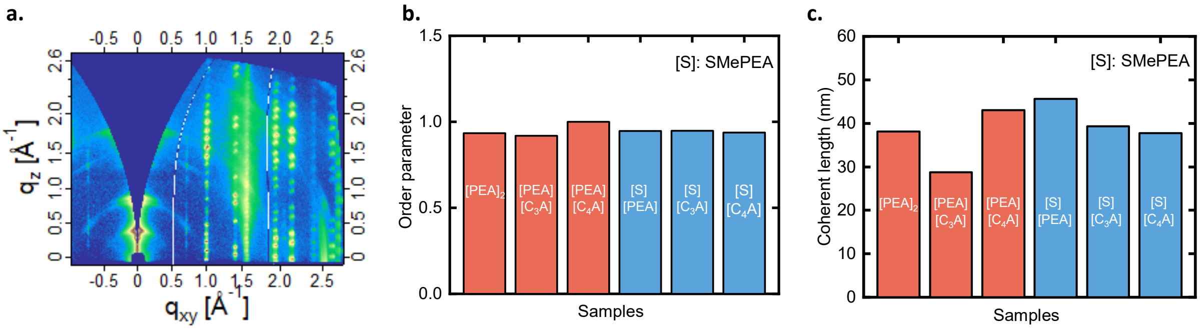

**Figure 5.** GIWAXS analysis of 2D HOIP thin films. **(a)** GIWAXS intensity map for the [PEA]$_2$ PbI$_4$ thin film. **(b)** Variation of the order parameter across 2D HOIP thin films based on the (010) scattering peak near 0.4 Å$^{-1}$. All the films show order parameters close to one, indicating near parallel orientation for all the films. **(c)** Variation of the coherent length across 2D HOIP thin films.

**Figure 5(a)** shows the diffraction intensity color map for the pure achiral [PEA]$_2$PbI$_4$ thin film. The localized high intensity spots in the color map are indicative of high crystallographic orientation of the 2D HOIP thin film. The GIWAXS color map of the rest of the six samples is shown in **Supplementary Figure S6**. **Figure 5(b)** shows that most films in this study show an order parameter value close to unity, which highlights the preferred parallel orientation of the 2D HOIP thin film relative to the substrate. The cross-plane thermal conductivity is typically lower in the case of parallel orientation, owing to the weaker non-bonded interactions.[56] This explains the lower thermal conductivity in our 2D HOIP thin films (~ 0.1 - 0.25 W m$^{-1}$ K$^{-1}$), relative to the 3D HOIP thin films.[37] **Figure 5(c)** shows the measured coherent length (crystallite size) of six 2D HOIP thin films extracted from the (010) peak near 0.4 Å$^{-1}$. Typically, the variation of the thermal conductivity with characteristic length (crystallite size in our case) is only significant when the characteristic length scale shrinks down to comparable to the phonon mean free path of the material.[50] Thermal conductivity in 2D HOIP is primarily contributed by phonons, which can be scattered at the inorganic layer, organic layer, inorganic-organic interface, and organic-organic interface in the unit cell, and then the nanocrystalline boundaries and film surfaces.[18,37]The phonon mean free path in hybrid 2D perovskites is roughly estimated to be less than 5 nm on average, which is understandable considering the organic and inorganic interfaces occur every 1-2 nm.[57,58] The crystallite size in our 2D HOIP thin films is about 40 nm (with the lowest one ≈29 nm), much larger than the phonon mean free path in the material and thus the variation in crystallite size (coherent length) should not have any apparent effect on the measured thermal conductivity. Therefore, the observed variation in thermal conductivity should be primarily attributed to the difference in the chemical composition, instead of the nanocrystal orientation and size in the polycrystalline texture.

### 3.2 Achiral 2D HOIP films: alkyl-alkyl interface *v.s.* aryl-aryl interface

For 2D HOIP films with achiral alkyl-alkyl organic interfaces, the correlation between thermal conductivity and elastic modulus is positive (i.e., thermal conductivity increases with increasing elastic modulus)[51], which agrees with that in 3D HOIPs[22], polymers[5,7], and amorphous macromolecules[6]. In other words, both thermal conductivity and elastic modulus decrease with a longer alkyl chain length, from [$C_4$A] to [$C_7$A]. In general, thermal conductivity in HOIPs is influenced by the phonon group velocity and scattering at the organic-organic interface.[18] As the latter is similar between the two for alkyl-type interface, the observed difference in thermal conductivity is primarily attributed to the difference in phonon group velocity. Past studies on hybrid perovskites have shown a significant contribution of acoustic phonons on thermal conductivity coupled with short optical phonon lifetimes, indicating direct correlation between sound velocity and phonon group velocity.[59–61] It has been demonstrated in the literature that elastic modulus (scales with sound velocity) shows a decrease from [$C_4$A]$_2$Pb$I_4$ to [$C_7$A]$_2$Pb$I_4$ owing to the replacement of softer and flexible organic layers with an increasing alkyl chain length.[23] We note that one previous investigation on 2D HOIP single crystals claimed to have no dependence of the alkyl chain length on thermal conductivity for alkyl-alkyl interfaces, contrary to our observation.[24] This discrepancy can be potentially explained considering structural rearrangement of the single crystals in their study due to high temperature rise (~30 K), differences in the preparation procedure and measurement conditions (e.g., prevention of degradation). Further, we also point out that the thermal conductivity result reported for [$C_4$A]$_2$Pb$I_4$ in their study is lower than our measurement and other studies, which again is potentially attributed to the structural changes due to steady-state heating during experiments and also the degradation.[24,38,62]

Next, we compare the measured thermal conductivity of [PEA]$_2$Pb$I_4$ (aryl-aryl interface), [$C_4$A]$_2$Pb$I_4$, and [$C_6$A]$_2$Pb$I_4$ (the latter two with alkyl-alkyl interface). The chain length in [PEA]$_2$Pb$I_4$ and [$C_4$A]$_2$Pb$I_4$ is similar whereas the interlayer distance in [PEA]$_2$Pb$I_4$ and [$C_6$A]$_2$Pb$I_4$ is similar. CR-AFM measurements of achiral 2D HOIPs in this work show that the elastic modulus for [PEA]$_2$Pb$I_4$ thin film is the highest (≈12 GPa), which is attributed to the rigidity of the benzene rings and the CH-π interaction.[39,40] The elastic modulus of [PEA]$_2$Pb$I_4$ is much higher (≈4 - 6 times) than that of [$C_4$A]$_2$Pb$I_4$ and [$C_6$A]$_2$Pb$I_4$.[39] Pure aryl-aryl interface (as in [PEA]$_2$Pb$I_4$) exhibits sp2 ($CH\cdots\pi$) interaction in addition to the weak van der Waals interaction in pure alkyl-alkyl interface, which was intuitively thought to offer additional heat transfer pathways for a stronger phonon transmission across the interface,[27] however, the opposite was observed in the measured result.[39] The observed low thermal conductivity in [PEA]$_2$Pb$I_4$ highlights the strong phonon scattering or filtering across the aryl-aryl interface. Our recent simulation work indicates that the thermal transport across the aryl-aryl interface, despite its stronger interaction strength (and thus a higher elastic modulus), is much weaker compared to the alkyl-alkyl interface counterpart, due to a reduced phonon density of states at the broad spectrum caused by the rigidity and large mass of the rings.[28]

### 3.3 Mixed achiral 2D HOIP films: alkyl-aryl interface

Replacing PEA with softer alkyl chains leads to a reduction of elastic modulus in the mixed achiral 2D HOIP films. And all the mixed-achiral 2D HOIP films have a larger elastic modulus compared to the their pure akyl counterpart (e.g., E≈2.1 GPa for [$C_6$A]Pb$I_4$ and E≈3.3 GPa for [$C_4$A]Pb$I_4$)[23]. Surpringly, the elastic modulus of [$C_3$A][PEA]Pb$I_4$ is smaller than [$C_4$A][PEA]Pb$I_4$ (**Figure 3(d)**), even though the former has alkyl chains that might be stiffer (i.e., $E_{C3A} > E_{C4A}$).[23,41] Given the comparable interlayer distance in the two mixed achiral 2D HOIPs, we speculate that the H-C distance between the ligands in [$C_4$A][PEA]Pb$I_4$ is shorter compared to $[C_3A][PEA]PbI_4$, as the alkyl chain length of $C_4A$ is larger than $C_3A$. Consequently, this implies that the CH-π interaction in $[C_4A][PEA]$ is stronger than in $[C_3A][PEA]$, potentially explaining higher elastic modulus in $[C_4A][PEA]PbI_4$. Furthermore, using a similar rationale, $[C_4A][PEA]PbI_4$ is expected to be more densely packed, indicative of a more rigid alkyl chain compared to $[C_3A][PEA]PbI_4$.[63]

Contrasting elastic modulus, thermal conductivity increases when replacing half of the aryl cations in $[PEA]_2PbI_4$ with alkyl cations such as $[C_3A]$ or $[C_4A]$. This increase highlights the difference and mismatch in the phonon modes between the alkyl and aryl groups. Our previous simulation work also suggests the presence of a much broader spectrum of phonon modes in alkyl groups in comparison to aryl groups.[28] The interlayer distance in $[C_3A][PEA]PbI_4$ and $[C_4A][PEA]PbI_4$ is nearly identical even though the alkyl chain length is different in these two, which implies that variation in alkyl chain length leads to a different structural packing and spacing between the organic cations (see **Figure 1(c)** for illustration). In these mixed 2D HOIPs, all three different types of interfaces (i.e., alkyl-alkyl, alkyl-aryl, and aryl-aryl) can transfer heat (see **Supplementary Figure S1**), and thus variation in the spacing can significantly affect the thermal conductivity (This is also elaborated in **Figure 6** for half-chiral 2D HOIPs). We speculate that both the aryl-aryl and aryl-alkyl organic interfaces contribute the heat transfer pathway in $[C_4A][PEA]PbI_4$, leading to a lower thermal conductivity than $[C_3A][PEA]PbI_4$, where possibly the alkyl-alkyl interface dominates the heat transfer pathway. However, due to the unavailability of structural data for mixed-achiral 2D HOIPs, this claim cannot be quantitively established. We do not observe any direct correlation between the interlayer distance and the thermal conductivity (see **Supplementary Section S5**), as also evidenced in other studies.[18,24,38]

### 3.4 Half-chiral 2D HOIP films

**Figure 2(d)** shows that thermal conductivity for all the half-chiral HOIPs (e.g., $[SMePEA][C_3A]PbI_4$, $[SMePEA][C_6A]PbI_4$) is similar, regardless of the interlayer distance and the achiral organic cation. This behavior can be explained by the unique structure and molecular packing of half-chiral 2D HOIPs. To start with, there are three potential heat transfer pathways in these structures including across alkyl-alkyl, alkyl-aryl, and aryl-aryl organic-organic interfaces, as illustrated in **Supplementary Figure S1(c)**. Thermal conductivity is thus proportional to the summation of all thermal conductances across the three interfaces, following the concept of thermal resistance network.[64,65] Our group has used this thermal resistance network concept to successfully explain the thermal transport in amorphous materials[64], liquids[65], and across interfaces[66,67]. To understand how the variation in molecular packing changes the relative contribution from the three heat transfer pathways, we calculated thermal conductance across the three types of interfaces as a function of spacing using non-equilibrium molecular dynamics (NEMD) simulations as a reference. The details regarding the NEMD simulation are described in **Methods** and **Supplementary Section S6**.

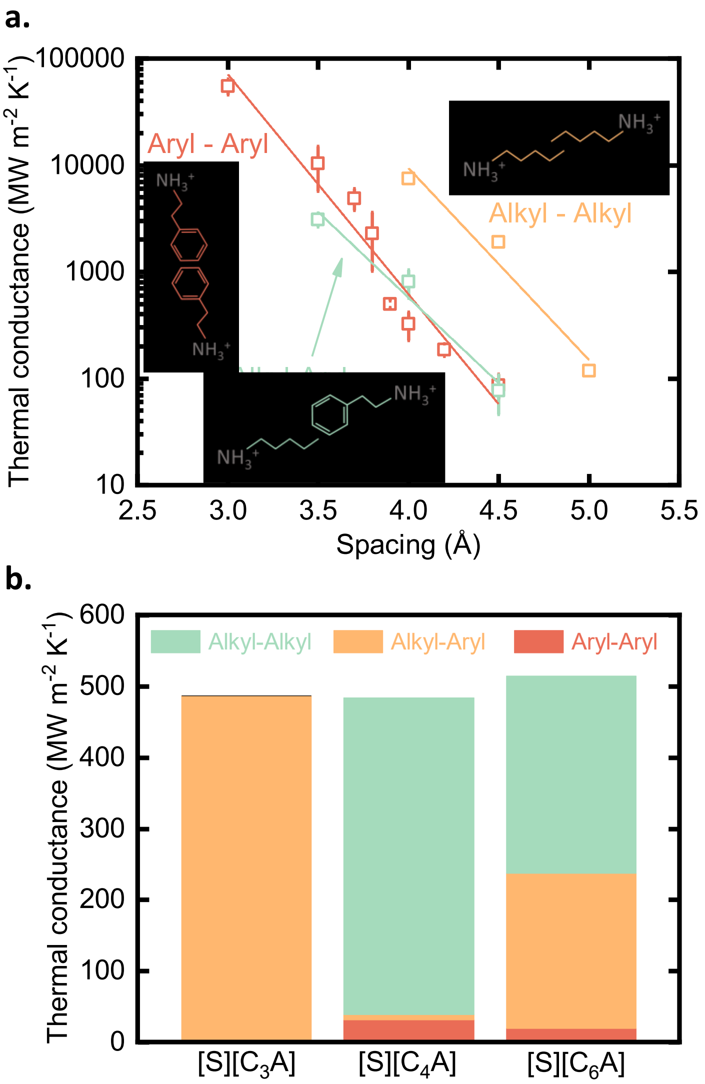

**Figure 6**. Molecular dynamics simulation results for understanding thermal conductance between different organic-organic interfaces. **(a)** Thermal conductance across three different types of interfaces as a function of organic-organic ligand spacing calculated using molecular dynamics simulations. The symbols indicate the computed thermal conductance, and the lines show the best linear fit. **(b)** Thermal conductance across each interface for [S][$C_3A$]$PbI_4$, [S][$C_4A$]$PbI_4$, and [S][$C_6A$]$PbI_4$ 2D HOIPs. [S] is short for [SMePEA].

**Figure 6(a)** shows the computed thermal conductance as a function of spacing (see **Figure 1(c)** for illustration). Note that the thermal conductance across alkyl-alkyl interface is significantly larger than the aryl-aryl and aryl-alkyl interface, emphasizing the role of aryl-aryl interaction on leading to a low thermal conductance and thus thermal conductivity. We examined three typical structures of [SMePEA][$C_3A$]$PbI_4$, [SMePEA][$C_4A$]$PbI_4$, and [SMePEA][$C_6A$]$PbI_4$ here. The spacing is obtained from the structural data for these three 2D HOIPs. To ensure the spacing from the structural data is correct, we also relaxed one of the structures at 300K and calculated the spacing, and we do not observe any noticeable difference between the relaxed and the original structure. Using the spacing and NEMD calculated thermal conductance data, we calculated the thermal conductances across each interface and summed them up in the three 2D HOIP structures for the cross-plane thermal conductivity as shown in **Figure 6(b)**. For a shorter alkyl chain length([SMePEA][$C_3A$]), the alkyl-aryl interface contributes to the total thermal conductivity the most. Increasing carbon chain length leads to a change in the packing of these organic cations, also making alkyl-alkyl interactions contributes to thermal transport. The contribution of the aryl-aryl interface to thermal transport is almost negligible compared to the other two interfaces. This is not surprising considering the rings tend to be isolated (large spacing) for structure stability. The total thermal conductance, however, is similar across the three 2D HOIPs, which is consistent with our thermal conductivity measurements. We believe that a similar trade off among thermal conductances across the three interfaces is responsible for the observed thermal conductivity trend for [SMePEA][PEA]$PbI_4$ and [SMePEA][$C_8$A]$PbI_4$.

For half-chiral films, their elastic moduli are similar within the experimental uncertainty, falling in between 7~9 GPa for all the films. This highlights the dominant effect of the chiral molecule in dictating the mechanical properties through their intermolecular interactions, regardless of the choice of the mixing organic cations and despite the small variations in the interlayer distance.

### 3.5 Full-chiral 2D HOIP films

Further, thermal conductivity of full-chiral 2D HOIPs (i.e., $[SMBA]_2PbI_4$ and $[SMePEA]_2PbI_4$) is higher than that of the half-chiral ones, even larger than the lowest thermal conductivity observed in achiral 2D HOIPs ($[PEA]_2PbI_4$). This comparison seems to indicate that the rings are more closely packed (smaller spacing) in full-chiral 2D HOIPs than the aryl-alkyl spacing and aryl-aryl spacing in half-chiral 2D HOIPs. This is also indicative of the importance of orientation of the rings in determining thermal transport across aryl-aryl type interface.[28] A notable difference between the structures of $[SMePEA]_2PbI_4$ and $[PEA]_2PbI_4$ is the presence of several diverse orientations of rings in the former. This may allow for several phonon modes to exist leading to a better thermal transport. Such tuning of thermal conductivity with different aryl-aryl orientations provides an avenue for future studies in these materials.

Compared to the pure achiral $[PEA]_2PbI_4$, the pure chiral $[SMePEA]_2PbI_4$ manifests a much lower elastic modulus ($\approx$ 7.3 GPa). Since the total number of the rigid rings is similar, the mechanical property contrast can be attributed to the differences in the interaction resulting from the orientation of rings and the variation in CH-$\pi$ interaction arising from the chiral structure. Comparing the structure of pure achiral $[PEA]_2PbI_4$ and pure chiral $[SMePEA]_2PbI_4$ suggests that in the former, every aryl cation participates in the CH-$\pi$ interaction, while in latter, only half of the aryl cation participates in the CH-$\pi$ interaction, as also observed in half-chiral and full-chiral 2D HOIPs.[26]

## 4. Conclusion

Through a detailed investigation of 12 different 2D metal halide HOIP thin films comprising achiral and chiral organic cations, we provide the first report of thermal conductivity and elastic modulus characterizations on mixed-achiral (e.g., [$C_4$A][PEA]$PbI_4$), half-chiral (e.g., [SMePEA][$C_6$A]$PbI_4$), and full-chiral (e.g., $[SMePEA]_2PbI_4$) 2D HOIP thin films. The highlight of this work is the discovery of anomalous correlations between thermal conductivity and elastic modulus in mixed-achiral and half-chiral 2D HOIPs:

(1) Mixing alkyl ligands with aryl ones, thermal conductivity of 2D HOIPs is suppressed due to the aryl-aryl and aryl-alkyl organic-organic interface while elastic modulus is enhanced by the CH-$\pi$ interactions at these interfaces and rigidity of organic cations.

(2) Introducing chirality into the 2D HOIP structure engenders unique structural changes that stabilize the thermal conductivity and elastic modulus regardless of the choice of achiral organic ligands.

Combining structural analysis, thermal conductivity characterization, elastic modulus measurement, and molecular dynamics simulation, this work offers insights into the structure-property relationship and highlights the importance of organic-organic interface in modulating thermal conductivity and elastic modulus, key parameters in implementing these materials at a device level.

## 5. Methods

### 5.1 Sample preparation

**Synthesis of ammonium iodide salts:** All ammonium iodide salts were synthesized by reaction of corresponding amine with unstabilized hydroiodic acid (HI) (57 wt% in water, Sigma-Aldrich). Before reaction, the hydroiodic acid was purified using a 0.36 M tributyl phosphate solution in chloroform, following a previously reported procedure.[68] Then fresh purified HI was dropped into a cold solution of amine in 10 mL ethanol under stirring in an ice bath. After 1 hour of stirring, the crude product was obtained by slowly evaporating the solvent under a reduced pressure. Then the white to light yellow precipitate was dissolved and recrystallized in ethanol and washed with ethyl ether three times. The product was dried under vacuum overnight and kept in a nitrogen gas filled glove box for further use.

**Deposition of perovskite films:** B doped p-type single side polished (100) Si substrates (University Wafer) with a resistivity of 1-10 Ω cm were cleaned with ultrasonic wave in deionized water, acetone, then 2-proponal for 15 minutes each. The substrates were dried under a stream of nitrogen and subjected to the treatment of UV-Ozone for 15 min. For pure ammonium cation based perovskite, the precursor solution was made by dissolving corresponding ammonium iodide salt and $PbI_2$ in DMF with the molar ratio of 2:1 and the solution was stirred at room temperature for 1 hour. The concentration of $Pb^{2+}$ is 0.3 M. For mixed cation based perovskite, the precursor solution was prepared by mixing previous pure ammonium cation based solution with 0.3M $Pb^{2+}$ with 1:1 volume ratio. The 2D perovskite film was obtained by spin-coating precursor solution at 5000 rpm for 20 s onto a precleaned Si substrate followed by thermal annealing at 80°C for 30 seconds.

### 5.2 Thermal conductivity characterization using TDTR

The thermal conductivity of 2D HOIP thin films was measured using the TDTR method. Prior to measurement, a thin layer of Al transducer (~ 80 nm) needs to be deposited. To protect the sensitive HOIP film from Al, an additional Cu layer (~ 20 nm) is deposited first on top of the 2D HOIP film prior to Al deposition. The precise thickness of the two metal layers is confirmed using picosecond acoustic method. In TDTR, a time delayed pump beam injects heat into the material, creating a time dependent temperature rise which is captured by the probe beam. The power (5 mW for both beams) and magnification (5× for both beams with a Gaussian beam size $\approx 12\ \mu m$) of the two beams is adjusted to ensure the temperature rise is within 10 K in the experiments. The samples are allowed to cool down for around 10 minutes before each TDTR scan. This is important to ensure the steady-state temperature rise in the material is low, to avoid any potential phase change or degradation in the 2D HOIP thin films. The experimental temperature rise is then fitted with a multilayered heat conduction model, with the thermal conductivity of 2D HOIP thin film as the only fitting parameter. The thermal properties of Si substrate, Cu and Al thin films are taken from literature.

### 5.3 Elastic modulus characterization using nanoindentation

CR-AFM is a dynamic AFM mode that utilizes the AFM cantilever resonance to measure the mechanical properties of materials, which has been widely used to quantify the elastic modulus of thin films, 2D materials, and single crystals.[69–73] In this study, all CR-AFM measurements were performed with an MFP-3D Infinity AFM (Asylum Research, an Oxford Instrument Company, CA) enclosed by a customized chamber under dry air flow (RH < 3%). Prior to the AFM measurements, the deflection sensitivity of the AFM cantilever (ZEILR, NanoWorld) was calibrated by force curves on a silicon surface freshly cleaned by Piranha solution (98% $H_2SO_4$ : 35% $H_2O_2$ = 3: 1 by volume).[70,72] The spring constant of the cantilever, $k_c$, was then calibrated by fitting the first free resonant peak to equations of a simple harmonic oscillator to measure the power spectral density of the thermal noise fluctuations in air.[74,75] The ultrasonic actuation of the AFM cantilever was achieved by gluing the perovskite thin film sample to an ultrasound transducer (V133-RM, Olympus NDT, see schematics in Figure 3(a)).[70–72] The dual actuation resonance tracking approach built in our MFP-3D Ininity AFM was used to track the CR frequency simultaneously during the contact mode topographic imaging and the total total applied force $F$ (including the adhesion force) during the scanning was also recorded.[72] The dynamic behavior of the AFM cantilever can be modeled as an Euler-Bernoulli beam oscillating with a mechanical constraint at the tip position (details can be found in Suppmentary Information Section S3) to extract the tip-sample contact stiffness $k^*$.[69,71,76] $k^*$ can then be converted to the reduced modulus (also called indentation modulus) $E^*$ of the tip-sample contact through contact mechanics models. Here, we employed the most-widely-used Hertzian contact model for the analysis, where the AFM tip-sample contact is approximated as a spherical indenter with a radius $R$ contacting a flat surface with a total force $F$:[69,71,76]

$$k^* = \sqrt[3]{6FRE^{*2}}. \tag{1}$$

$E^*$ can then be used to derive the material's elastic modulus by:

$$\frac{1}{E^*} = \frac{1-\upsilon_s^2}{E_s} + \frac{1-\upsilon_t^2}{E_t}, \tag{2}$$

where $E_s$ and $E_t$ are the Young's moduli, and $\upsilon_s$ and $\upsilon_t$ are the Poisson's ratios of the sample and the tip (silicon in this case), respectively. The tip position on the cantilever and the tip radius $R$ were calibrated by CR-AFM measurements on a sample with known stiffness (see Suppmentary Information Section S3 for more details).

### 5.4 GIWAXS characterization

GIWAXS experiments were performed on predeposited films at the BL 7.3.3. beamline of the Advanced Light Source (ALS), Lawrence Berkeley National Laboratory.[77] The samples were placed in a He-filled compartment during the measurements to minimize air scattering and beam damage. An X-ray beam of energy 10 keV was incident on the samples and the incidence angle was varied from 0.15° to 0.30° to determine the critical angle for total external reflection. The 2D data were recorded with a Pilatus 2M detector with a pixel size of 172 μm and placed at a distance of about 280 mm from the samples. The sample to detector distance was calibrated using the scattering pattern of a polycrystalline silver behenate (AgBH) calibration sample. To ensure that the bulk of the film is sampled, the incidence angle of 0.30° was chosen for all the analysis in this work. Data were analyzed using the Nika package for Igor Pro software (Wavemetrics Inc.).[78] Sector-averaged 1D in-plane and out-of-plane scattering profiles were computed using 10° wide cake slices from the 2D diffraction patterns. The diffraction peaks in the 1D profiles were fitted using Voigt functions on a polynomial background. Coherent lengths were obtained by applying the Scherrer grain size analysis to the fitted peaks.[79] Peaks were assigned to crystal facets by comparing the experimental data to simulated X-ray diffraction pattern (see Supplementary Information for details). Volume normalized geometry corrected pole figures were obtained from the missing wedge corrected 2D GIWAXS images.[80] The isotropic background was subtracted from the pole figure profiles using a linear interpolation of pre-peak and post-peak intensities. The polar angle ($\chi$) is defined as the angle of the measured scattering signal from the normal to the substrate. Therefore, $\chi = 0°$ is perpendicular to the plane of the substrate, and $\chi = 90°$ is parallel to the plane of the substrate or the horizon. The measure of orientation distribution of crystallites was obtained by the calculating order parameter for the (010) peak near 0.4 Å$^{-1}$. The order parameter ($S$) is related to the second moment orientation distribution by the equation:[81]

$$S = \frac{1}{2}(3\langle \cos^2 \chi \rangle - 1) \tag{3}$$

The second moment of the orientation distribution was calculated from the measured intensity $I(\chi)$ using the relation:

$$\langle \cos^2 \chi \rangle = \frac{\int_0^{\pi/2} I(\chi) \cos^2 \chi \sin \chi d\chi}{\int_0^{\pi/2} I(\chi) \sin \chi d\chi} \tag{4}$$

### 5.5 Thermal conductance calculation using MD simulations

We conducted non-equilibrium MD simulations in the LAMMPS software package. We chose poly(p-phenylene) (PPP) as a prototypical polymer to model the thermal conductance across aryl-aryl interface. We chose polyethylene (PE) to model the thermal conductance across alkyl-alkyl interface. We used Polymer Consistent Force Field (PCFF) to model the interatomic potential with a cutoff distance of 10 Angstrom. The simulation box consists of multiple polymer chains separated by a predetermined spacing, varied between 4 – 6 Angstrom. More details about the simulation setup are described in Suppmentary Information Section S5 and can be also found in our previous publication[28].

## Acknowledgements

J.L. acknowledges the primary financial support from National Science Foundation under the award number CBET-1943813, to support the work by graduate students A.N., C.Y., S.R., and Z.W.. Q.T. acknowledges the support from the National Science Foundation under the award number CMMI-2311573, for the elastic modulus measurements, done by graduate students Y.Y., D.K.. L.Y. and W.Y. acknowledge the support from the National Science Foundation under the award number CHE-2154791. S.M. and H.A. acknowledge ONR grant N000142012155 and Goodnight Innovation Dist. Professor Endowment for X-ray data acquisition. GIWAXS data were acquired at the beamline BL 7.3.3. of the Advanced Light Source, which is supported by the Director, Office of Science, Office of Basic Energy Sciences, of the U.S. Department of Energy under Contract DE-AC02-05CH11231. Eric Schaible (BL7.3.3, ALS) is gratefully acknowledged for beamline maintenance as well as assistance with GIWAXS experiments. D.S. acknowledges the financial support from the Department of Energy under the award number DE-SC0020992, for the device fabrication done by A.H.C. Computational resources were provided by the High-Performance Computing Center at North Carolina State University and the Advanced Cyberinfrastructure Coordination Ecosystem: Service & Support (ACCESS) program, which is supported by NSF grants 2138259, 2138286, 2138307, 2137603, and 2138296.

## Data Availability

The data that support the findings of this study are available upon reasonable request from the corresponding authors.

## Conflict of Interest

The authors declare no competing interest.

## References

[1] P. Holzhey, M. Saliba, *J. Mater. Chem. A* **2018**, *6*, 21794–21808.

[2] B. Conings, J. Drijkoningen, N. Gauquelin, A. Babayigit, J. D'Haen, L. D'Olieslaeger, A. Ethirajan, J. Verbeeck, J. Manca, E. Mosconi, F. De Angelis, H.-G. Boyen, *Adv. Energy Mater.* **2015**, *5*, 1500477.

[3] X. Zhao, T. Liu, Y. L. Loo, *Adv. Mater.* **2022**, *34*, 2105849.

[4] D. G. Cahill, S. K. Watson, R. O. Pohl, *Phys. Rev. B* **1992**, *46*, 6131–6140.

[5] X. Xie, D. Li, T.-H. Tsai, J. Liu, P. V Braun, D. G. Cahill, *Macromolecules* **2016**, *49*, 972–978.

[6] X. Xie, K. Yang, D. Li, T.-H. Tsai, J. Shin, P. V Braun, D. G. Cahill, *Phys. Rev. B* **2017**, *95*, 35406.

[7] J. Liu, X. Wang, D. Li, N. E. Coates, R. A. Segalman, D. G. Cahill, *Macromolecules* **2015**, *48*, 585–591.

[8] T. Ghosh, M. Dutta, D. Sarkar, K. Biswas, *J. Am. Chem. Soc.* **2022**, *144*, 10099–10118.

[9] X. Qian, J. Zhou, G. Chen, *Nat. Mater.* **2021**, *20*, 1188–1202.

[10] M. Beekman, D. G. Cahill, *Cryst. Res. Technol.* **2017**, *52*, 1700114.

[11] M. Roufosse, P. G. Klemens, *Phys. Rev. B* **1973**, *7*, 5379–5386.

[12] Z. Q. Ma, Y. Shao, P. K. Wong, X. Shi, H. Pan, *J. Phys. Chem. C* **2018**, *122*, 5844–5853.

[13] G. Grancini, M. K. Nazeeruddin, *Nat. Rev. Mater.* **2019**, *4*, 4–22.

[14] S. Herculano-Houzel, *Science (80-. ).* **2013**, *342*, 316–317.

[15] S. Parola, B. Julián-López, L. D. Carlos, C. Sanchez, *Adv. Funct. Mater.* **2016**, *26*, 6506–6544.

[16] S. D. Stranks, H. J. Snaith, *Nat. Nanotechnol.* **2015**, *10*, 391–402.

[17] S. Sourisseau, N. Louvain, W. Bi, N. Mercier, D. Rondeau, F. Boucher, J. Y. Buzaré, C. Legein, *Chem. Mater.* **2007**, *19*, 600–607.

[18] M. A. Haque, S. Kee, D. R. Villalva, W. L. Ong, D. Baran, *Adv. Sci.* **2020**, *7*, 1903389 [19] L. N. Quan, M. Yuan, R. Comin, O. Voznyy, E. M. Beauregard, S. Hoogland, A. Buin, A. R. Kirmani, K. Zhao, A. Amassian, D. H. Kim, E. H. Sargent, *J. Am. Chem. Soc.* **2016**, *138*, 2649–2655.

[20] K. Z. Du, Q. Tu, X. Zhang, Q. Han, J. Liu, S. Zauscher, D. B. Mitzi, *Inorg. Chem.* **2017**, *56*, 9291–9302.

[21] J. Azadmanjiri, J. Wang, C. C. Berndt, A. Yu, *J. Mater. Chem. A* **2018**, *6*, 3824–3849.

[22] G. A. Elbaz, W. L. Ong, E. A. Doud, P. Kim, D. W. Paley, X. Roy, J. A. Malen, *Nano Lett.* **2017**, *17*, 5734–5739.

[23] Q. Tu, I. Spanopoulos, S. Hao, C. Wolverton, M. G. Kanatzidis, G. S. Shekhawat, V. P. Dravid, *ACS Appl. Mater. Interfaces* **2018**, *10*, 22167–22173.

[24] M. A. J. Rasel, A. Giri, D. H. Olson, C. Ni, P. E. Hopkins, J. P. Feser, *ACS Appl. Mater. Interfaces* **2020**, *12*, 53705–53711.

[25] L. Yan, C. J. Gloor, A. M. Moran, W. You, **2023**, *Appl. Phys. Lett.* **2023,** *122,*240501.

[26] L. Yan, M. K. Jana, P. C. Sercel, D. B. Mitzi, W. You, *J. Am. Chem. Soc.* **2021**, *143*, 18114–18120.

[27] L. Yan, J. Hu, N. Zhou, A. M. Moran, W. You, *Sol. RRL* **2020**, *4*, 1900374.

[28] C. Yang, S. Raza, X. Li, J. Liu, *J. Phys. Chem. B* **2023**, *127*, 6804–6813.

[29] J. Qiu, Y. Xia, Y. Zheng, W. Hui, H. Gu, W. Yuan, H. Yu, L. Chao, T. Niu, Y. Yang, X. Gao, Y. Chen, W. Huang, *ACS Energy Lett.* **2019**, *4*, 1513–1520.

[30] N. Zhou, B. Huang, M. Sun, Y. Zhang, L. Li, Y. Lun, X. Wang, J. Hong, Q. Chen, H. Zhou, *Adv. Energy Mater.* **2020**, *10*, 1–13.

[31] X. Lian, J. Chen, M. Qin, Y. Zhang, S. Tian, X. Lu, G. Wu, H. Chen, *Angew. Chemie - Int. Ed.* **2019**, *58*, 9409–9413.

[32] A. Pietropaolo, A. Mattoni, G. Pica, M. Fortino, G. Schifino, G. Grancini, *Chem* **2022**,

*8*, 1231–1253.
[33] J. Ma, H. Wang, D. Li, *Adv. Mater.* **2021**, *33*, 2008785.
[34] K. Kim, E. Vetter, L. Yan, C. Yang, Z. Wang, R. Sun, Y. Yang, A. H. Comstock, X. Li, J. Zhou, L. Zhang, W. You, D. Sun, J. Liu, *Nat. Mater.* **2023**, *22*, 322–328.
[35] A. D. Christodoulides, P. Guo, L. Dai, J. M. Hoffman, X. Li, X. Zuo, D. Rosenmann, A. Brumberg, M. G. Kanatzidis, R. D. Schaller, J. A. Malen, *ACS Nano* **2021**, *15*, 4165–4172.
[36] S. Thakur, Z. Dai, P. Karna, N. P. Padture, A. Giri, *Mater. Horizons* **2022**, *9*, 3087–3094.
[37] Y. Jung, W. Lee, S. Han, B. S. Kim, S. J. Yoo, H. Jang, *Adv. Mater.* **2023**, *2204872*
[38] A. Giri, A. Z. Chen, A. Mattoni, K. Aryana, D. Zhang, X. Hu, S.-H. Lee, J. J. Choi, P. E. Hopkins, *Nano Lett.* **2020**, *20*, 3331–3337.
[39] Q. Tu, I. Spanopoulos, E. S. Vasileiadou, X. Li, M. G. Kanatzidis, G. S. Shekhawat, V. P. Dravid, *ACS Appl. Mater. Interfaces* **2020**, *12*, 20440–20447.
[40] H. Gao, W. Wei, L. Li, Y. Tan, Y. Tang, *J. Phys. Chem. C* **2020**, *124*, 19204–19211.
[41] I. Spanopoulos, I. Hadar, W. Ke, Q. Tu, M. Chen, H. Tsai, Y. He, G. Shekhawat, V. P. Dravid, M. R. Wasielewski, A. D. Mohite, C. C. Stoumpos, M. G. Kanatzidis, *J. Am. Chem. Soc.* **2019**, *141*, 5518–5534.
[42] M. A. Reyes-Martinez, P. Tan, A. Kakekhani, S. Banerjee, A. A. Zhumekenov, W. Peng, O. M. Bakr, A. M. Rappe, Y.-L. Loo, *ACS Appl. Mater. Interfaces* **2020**, *12*, 17881–17892.
[43] Q. Tu, D. Kim, M. Shyikh, M. G. Kanatzidis, *Matter* **2021**, *4*, 2765–2809.
[44] L. Mao, C. C. Stoumpos, M. G. Kanatzidis, *J. Am. Chem. Soc.* **2019**, *141*, 1171–1190.
[45] J. Liu, B. Yoon, E. Kuhlmann, M. Tian, J. Zhu, S. M. George, Y.-C. Lee, R. Yang, *Nano Lett.* **2013**, *13*, 5594–5599.
[46] J. Liu, J. Zhu, M. Tian, X. Gu, A. Schmidt, R. Yang, *Rev. Sci. Instrum.* **2013**, *84*, 034902.
[47] S. Wang, X. Lu, A. Negi, J. He, K. Kim, H. Shao, P. Jiang, L. Jun, Q. Hao, *Eng. Sci.* **2022**, *17*, 45–55.
[48] K. Chatterjee, A. Negi, K. Kim, J. Liu, T. K. Ghosh, *ACS Appl. Energy Mater.* **2020**, *3*, 6929–6936.
[49] H. Subramanyan, K. Kim, T. Lu, J. Zhou, J. Liu, *AIP Adv.* **2019**, *9*, 115116.
[50] A. Negi, A. Rodriguez, X. Zhang, A. H. Comstock, C. Yang, *Adv. Sci.* **2023**, *2301273*, 1–10.
[51] E. Isotta, W. Peng, A. Balodhi, A. Zevalkink, *Angew. Chemie - Int. Ed.* **2023**, *62*, e202213649.
[52] G. A. Elbaz, W.-L. Ong, E. A. Doud, P. Kim, D. W. Paley, X. Roy, J. A. Malen, *Nano Lett.* **2017**, *17*, 5734–5739.
[53] Z. Tian, J. Garg, K. Esfarjani, T. Shiga, J. Shiomi, G. Chen, *Phys. Rev. B - Condens. Matter Mater. Phys.* **2012**, *85*, 184303.
[54] S. Mukhopadhyay, L. Lindsay, D. J. Singh, *Sci. Rep.* **2016**, *6*, 37076.
[55] P. Acharyya, T. Ghosh, K. Pal, K. Kundu, K. Singh Rana, J. Pandey, A. Soni, U. V. Waghmare, K. Biswas, *J. Am. Chem. Soc.* **2020**, *142*, 15595–15603.
[56] C. Li, H. Ma, T. Li, J. Dai, M. A. J. Rasel, A. Mattoni, A. Alatas, M. G. Thomas, Z. W. Rouse, A. Shragai, S. P. Baker, B. J. Ramshaw, J. P. Feser, D. B. Mitzi, Z. Tian, *Nano Lett.* **2021**, *21*, 3708–3714.
[57] W. Lee, H. Li, A. B. Wong, D. Zhang, M. Lai, Y. Yu, Q. Kong, E. Lin, J. J. Urban, J. C. Grossman, P. Yang, *Proc. Natl. Acad. Sci. U. S. A.* **2017**, *114*, 8693–8697.
[58] S. Y. Yue, X. Zhang, G. Qin, J. Yang, M. Hu, *Phys. Rev. B* **2016**, *94*, 115427.
[59] L. D. Whalley, J. M. Skelton, J. M. Frost, A. Walsh, *Phys. Rev. B* **2016**, *94*, 220301.
[60] T. Haeger, R. Heiderhoff, T. Riedl, *J. Mater. Chem. C* **2020**, *8*, 14289–14311.

[61] T. Handa, T. Yamada, M. Nagai, Y. Kanemitsu, *Phys. Chem. Chem. Phys.* **2020**, *22*, 26069–26087.

[62] Q. Wang, Z. Zeng, Y. Chen, *Phys. Rev. B* **2021**, *104*, 1–6.

[63] C. J. Dahlman, R. M. Kennard, P. Paluch, N. R. Venkatesan, M. L. Chabinyc, G. N. Manjunatha Reddy, *Chem. Mater.* **2021**, *33*, 642–656.

[64] J. Zhou, Q. Xi, J. He, X. Xu, T. Nakayama, Y. Wang, J. Liu, *Phys. Rev. Mater.* **2020**, *4*, 015601.

[65] D. Huang, J. Zhong, S. Raza, R. Niu, B. Fu, D. Yu, T. Nakayama, J. Liu, J. Zhou, *J. Phys. Condens. Matter* **2023**, *35*, 415101.

[66] X. Duan, Z. Li, J. Liu, G. Chen, X. Li, *J. Appl. Phys.* **2019**, *125, 164303*

[67] Y. Wu, X. Zhang, A. Negi, J. He, G. Hu, S. Tian, J. Liu, *Polymers (Basel).* **2020**, *12*, 426.

[68] I. C. Smith, E. T. Hoke, D. Solis-Ibarra, M. D. McGehee, H. I. Karunadasa, *Angew. Chem. Int. Ed. Engl.* **2014**, *53*, 11232–11235.

[69] U. Rabe, in (Eds.: B. Bhushan, H. Fuchs), Springer Berlin Heidelberg, Berlin, Heidelberg, **2006**, pp. 37–90.

[70] Q. Tu, H. S. Kim, T. J. Oweida, Z. Parlak, Y. G. Yingling, S. Zauscher, *ACS Appl. Mater. Interfaces* **2017**, *9*, 10203–10213.

[71] S. Zauscher, Z. Parlak, Q. Tu, *Handbook of nanomaterials properties*, 2014, 1023-1051 [72] Q. Tu, B. Lange, Z. Parlak, J. M. J. Lopes, V. Blum, S. Zauscher, *ACS Nano* **2016**, *10*, 6491–6500.

[73] W. Tang, T. Yang, C. A. Morales-Rivera, X. Geng, V. K. Srirambhatla, X. Kang, V. P. Chauhan, S. Hong, Q. Tu, A. J. Florence, H. Mo, H. A. Calderon, C. Kisielowski, F. C. R. Hernandez, X. Zou, G. Mpourmpakis, J. D. Rimer, *Nat. Commun.* **2023**, *14*, 561.

[74] J. L. Hutter, J. Bechhoefer, *Rev. Sci. Instrum.* **1993**, *64*, 1868–1873.

[75] D. A. Walters, J. P. Cleveland, N. H. Thomson, P. K. Hansma, M. A. Wendman, G. Gurley, V. Elings, *Rev. Sci. Instrum.* **1996**, *67*, 3583–3590.

[76] U. Rabe, S. Amelio, E. Kester, V. Scherer, S. Hirsekorn, W. Arnold, *Ultrasonics* **2000**, *38*, 430–437.

[77] A. Hexemer, W. Bras, J. Glossinger, E. Schaible, E. Gann, R. Kirian, A. MacDowell, M. Church, B. Rude, H. Padmore, *J. Phys. Conf. Ser.* **2010**, *247*, 012007.

[78] J. Ilavsky, *J. Appl. Crystallogr.* **2012**, *45*, 324–328.

[79] D. M. Smilgies, *J. Appl. Crystallogr.* **2009**, *42*, 1030–1034.

[80] J. L. Baker, L. H. Jimison, S. Mannsfeld, S. Volkman, S. Yin, V. Subramanian, A. Salleo, A. P. Alivisatos, M. F. Toney, *Langmuir* **2010**, *26*, 9146–9151.

[81] M. R. Hammond, R. J. Kline, A. A. Herzing, L. J. Richter, D. S. Germack, H.-W. Ro, C. L. Soles, D. A. Fischer, T. Xu, L. Yu, M. F. Toney, D. M. DeLongchamp, *ACS Nano* **2011**, *5*, 8248–8257.